Accepted Manuscript

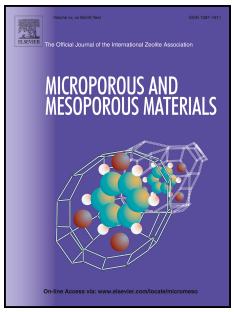

Optical quality mesoporous alumina thin films

Andrés Zelcer, Leila M. Saleh Medina, Pablo A. Hoijemberg, M. Cecilia Fuertes

PII: S1387-1811(19)30305-1

DOI: https://doi.org/10.1016/j.micromeso.2019.05.006

Reference: MICMAT 9481

To appear in: *Microporous and Mesoporous Materials*

Received Date: 15 February 2019

Revised Date: 17 April 2019

Accepted Date: 5 May 2019

Please cite this article as: André. Zelcer, L.M. Saleh Medina, P.A. Hoijemberg, M.C. Fuertes, Optical quality mesoporous alumina thin films, *Microporous and Mesoporous Materials* (2019), doi: https://doi.org/10.1016/j.micromeso.2019.05.006.

This is a PDF file of an unedited manuscript that has been accepted for publication. As a service to our customers we are providing this early version of the manuscript. The manuscript will undergo copyediting, typesetting, and review of the resulting proof before it is published in its final form. Please note that during the production process errors may be discovered which could affect the content, and all legal disclaimers that apply to the journal pertain.

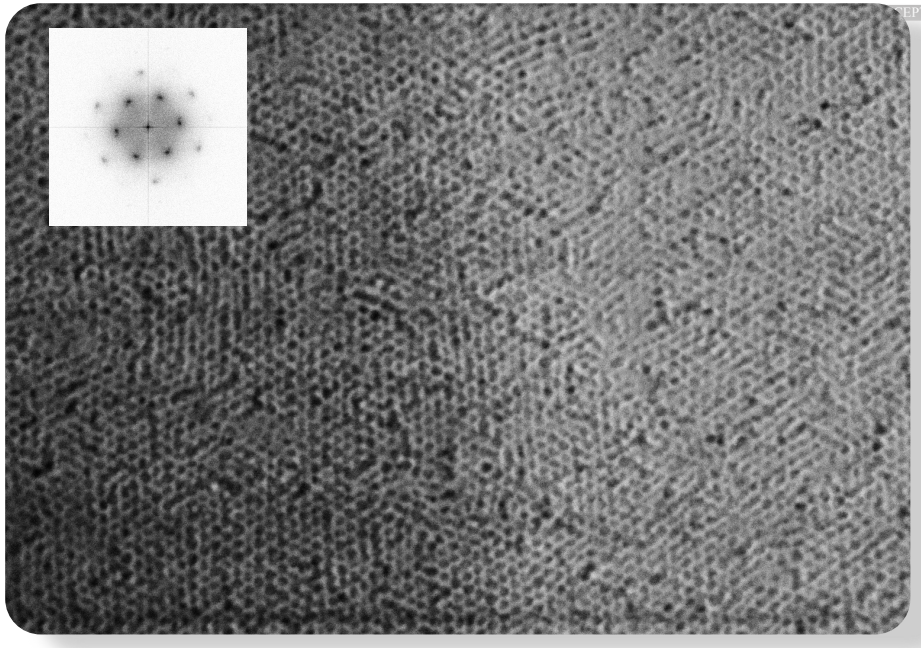

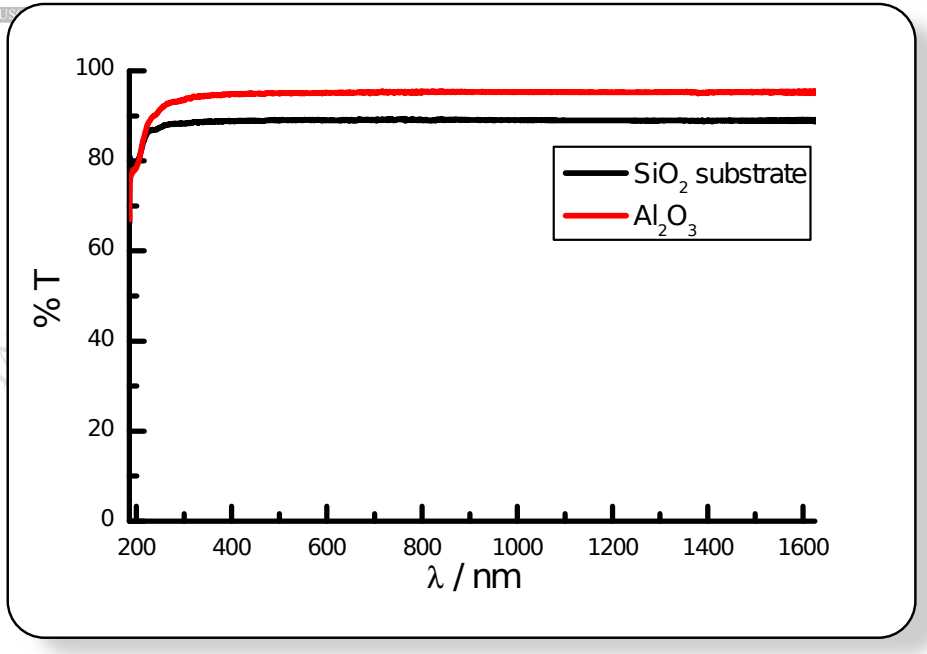

Highly ordered porosity

UV-Vis-NIR transparency

ACCEPTED MANUSCRIPT

Optical quality mesoporous alumina thin films

Andrés Zelcer[a,b,*], Leila M. Saleh Medina[a], Pablo A. Hoijemberg[a,b], M. Cecilia Fuertes[c]

[a] *CIBION, CONICET, Godoy Cruz 2390 (C1425FQD), CABA, Argentina. Tel: 5411 4899 5500*
[b] *ECyT-UNSAM, 25 de Mayo y Francia (1650), San Martín, Buenos Aires, Argentina.*
[c] *Gerencia Química-CAC-CNEA, CONICET, Avda. Gral. Paz 1499 (B1650KNA), San Martín, Buenos Aires, Argentina. and Instituto Sabato, Avda. Gral. Paz 1499 (B1650KNA), San Martín, Buenos Aires, Argentina.*

Abstract

A robust method for the preparation of optical-quality mesoporous alumina thin films is presented, using evaporation induced self assembly of triblock copolymer surfactants. The use of lowly reactive aluminium chloride as a precursor and a tertiary alcohol as a novel chloride scavenger results in highly homogeneous and smooth films with consistent controllable thickness between 30 and 100 nm. The films show very low refractive index and high transparency from UV to NIR regions, providing a new building block for solution processing of devices requiring low-κ materials.

Keywords:
Mesoporous thin films, UV transparent films, Sol-gel, Alumina

1. Introduction

Mesoporous materials have attracted attention from the materials science community since the discovery of simple and reproducible synthetic methods for their preparation. Their unique properties of accessibility and high surface area make them outstanding functional materials for sieving, sorption, catalysis and sensors.[1] When casted as thin films, mesoporous materials can be used as sieves and as building blocks of more complex systems and devices.[2] The huge potential of these materials pushed research towards new synthetic methods and the study of their physicochemical properties.[3]

One of the most versatile and widespread methods for preparing thin mesoporous films, mainly of metallic oxides, is termed Evaporation Induced Self Assembly (EISA).[4, 5] In this approach, sol-gel reactions are combined with the assembly of micelles that serve as sacrificial templating agents. Typically, solvent evaporation from a sol containing surfactant triggers micelle assembly and gelification of the precursors around the micelles. Further consolidation steps and template removal lead to a porous material, with pore sizes and ordering determined mainly by the micelle characteristics. Successful development of EISA

*Corresponding author
Email address: Andres.Zelcer@cibion.conicet.gov.ar (Andrés Zelcer)

processes requires precise adjustment of the hydrolysis and condensation kinetics in order to obtain stable sols and to allow the lyotropic mesophase formed by the surfactant micelles in the sol to develop.

Although initial development on mesoporous materials was mainly carried on silica, the interest on realizing mesoporous materials with different chemical, mechanical and optical properties led to the extension to hybrid materials, carbon and metal oxides.[6, 3, 7, 8] Among non-siliceous oxides, alumina is a ubiquous material since it is mechanically robust and it withstands high temperatures and aggressive chemical conditions. These characteristics, together with its acidic properties, make mesoporous alumina an important material as catalyst and catalyst support, particularly in the petroleum industry.[9] Processed as thin films, the inertness, low dielectric constant and low conductivity of mesoporous alumina enable its use in electrical and optical devices,[10] as well as in membranes, barriers, sensors, etc.[11]

Mesoporous thin films find applications as building blocks both for electronic devices, as insulating low-κ materials, and for optical devices. In this latter case, transparent films of controlled thickness and defined refractive index are needed. Specific applications include responsive 1D photonic crystals for sensing, energy generation[12] and antireflective coatings.[13] These devices are built stacking thin films of well defined optical path length; therefore the need for controlled thicknesses and refractive index. Materials currently used for the design and construction of such devices include mainly titania and zirconia, as high-refractive index materials, and silica, as a low-refractive index material. The availability of different materials widens the choice of available refractive indexes, and enables the design of advanced photonic sensors that profit from different surface chemistry of the materials. The incorporation of mesoporous aluminium oxides and oxohydroxydes thin films into the design of optical devices shows huge potential, since their refractive indexes are similar to that of silica but their chemistry is different. Nevertheless, most of the reported thin films deposition methods do not allow a precise and reproducible control of the thickness of the films. Methods that were developed for xerogels preparation usually do not perform as well when applied to thin films. The rates of evaporation and water exchange with the environment during film and bulk sample preparations are very different, producing significant differences in the sol-gel chemistry and EISA processes.

Aluminium shows a rich and complex hydrolytic chemistry in water. Many aluminium species exist in solution, with different degrees of hydrolysis and condensation. Aluminium sols behaviour depends on many conditions: pH, temperature, concentration, etc. Furthermore, many different alumina solid phases exist and several factors determine which phase is formed through sol-gel chemistry. Due to the nature of aluminium sol-gel chemistry, controlled reaction conditions are required to manage hydrolysis and condensation for thin film preparation. Particularly, the acidity of the sols has to be low enough to prevent extensive condensation and precipitation, yet not so low as to hinder gelation shortly after being deposited as thin films. In this work we use *tert*-butanol as a stable scavenger. This reagent has already been used to prepare titania sols[14] and, unlike epoxides, is stable at ambient conditions and in dilute acidic solutions. The reactivity of this alcohol is adequate to maintain a low pH until the EISA process takes place, resulting in sols that are stable

for longer periods. Moreover, compared to other reagents that work as bases like ammonia or epoxides, it is much easier to handle, being less toxic and less reactive. The thickness of the films prepared using this method is controllable and reproducible, and the excellent homogeneity of the films leads to outstanding transparency over a large wavelength range.

2. Experimental

2.1. Reagents and materials

$AlCl_3 \cdot 6\,H_2O$ was purchased from Merck. *tert*-butanol (*t*-BuOH) was provided by Mallinkrodt. Citric acid monohydrate (HCit) was acquired from Riedel-de Haën. Triblock copolymers Pluronic® F127 (Mw 13600) and P123 (Mw 5800) were purchased from Sigma–Aldrich. Absolute ethanol (Merck or BioPack) was used in all preparations. Deionized water was obtained from a Barnstead MicroPure system (Thermo Scientific). All reagents were used without further purification.

Glass (Merrienfield), silicon and fused silica (University Wafers) substrates were first thoroughly cleaned with water and ethanol, and finally treated with air plasma (Zepto, Diener GmbH) right before deposition.

2.2. Sol preparation

Sols were prepared by mixing $AlCl_3 \cdot 6\,H_2O$, H_2O, *t*-BuOH, EtOH, HCit and the surfactant in final proportions 1:20:3:x:0.25:s. The solvent proportion x was varied between 40 and 100, while the surfactant to aluminium relation s was varied between 0.002 and 0.006 for F127 and 0.014 and 0.019 for P123. The minimal proportion to obtain well-ordered pores was found to be 0.018 for P123 and 0.006 for F127, and was used throughout the rest of this work. To prepare the solutions, first $AlCl_3 \cdot 6\,H_2O$ was dissolved in water, then *t*-BuOH was added and the solution was heated at 50 °C for 15 min. The solution turned milky on heating and two phases developed. After cooling, a single phase is recovered. A solution of citric acid monohydrate on ethanol was then added. Finally, the desired amount of surfactant was incorporated. The solution was stirred after each addition until total dissolution or homogeneous mixing was observed. The addition of P123 is more conveniently performed dissolving the surfactant beforehand in a small portion of the required amount of ethanol.

2.3. Film deposition and treatment

Films were deposited by dip or spin coating on glass, fused silica or silicon substrates. Dip coating was performed on a homemade dip-coater, at withdrawal speeds ranging from 0.5 to 4.0 $mm \cdot s^{-1}$. The relative humidity (RH) during dip coating was maintained between 37 and 50 %. Spin coating was performed on a Laurell WS–650 MZ–23NPP spin-coater, using final angular velocities ranging from 2000 to 8000 rpm. The spinner was continuously purged with dry air, thus the RH inside the chamber was below 10 %RH.

After deposition some samples were directly subjected to thermal treatment, while others were first stored at room temperature and 50 %RH for 24 h and then thermally treated. The thermal treatment consisted on a first step at 60 °C for 24 h, then a second step at 130 °C for the same time and a final calcination step by heating at a rate of 1 °C·min^{-1} up to 350 °C

and maintaining the temperature for 2 h. Selected samples were heated in a tube furnace for short times at 1000 °C to achieve crystallization. Other thermal treatments performed are discussed below.

2.4. Characterization

Film morphology and pore ordering were observed by Field Emission Scanning Electron Microscopy (FESEM) using a SEM ZEISS LEO 982 GEMINI (CMA, FCEyN-UBA) operating at 5 kV. Pore ordering was also studied by Small Angle X-ray Scattering (SAXS) at the SAXS beamline of Elettra Sincrotrone (Trieste, Italy) using 8 keV radiation and a sample to detector distance of 828.81 mm, and by Grazing Incidence Small Angle X-ray Scattering (GISAXS)[15] on a Xenocs Xeuss 1.0 (INIFTA-CONICET, Argentina) using CuKα radiation and a sample to detector distance of 548.44 mm. In both cases a Pilatus 100K detector was employed.

Film thicknesses and porosities were measured by X-ray reflectometry (XRR) using a Panalytical Empyrean diffractometer, and by ellipsometry using a Sopra GE-5A spectroscopic ellipsometer (GQ–CAC–CNEA) using the software Winelli II 2.2.0.7. The porosity was estimated from XRR data by measuring the change of the critical angle when the RH changed from less than 5% to over 95%.[16] Pore size distribution was evaluated by Environmental Ellipsometric Porosimetry (EEP). This technique relates the changes on thickness and refractive index of a porous film measured at different RH to the amount of adsorbed water on the pores. The pore size distribution is then derived from the amount of adsorbed water using standard porosimetry formalisms. Full details on this technique can be found elsewhere.[17]

Grazing Incidence X–Ray Diffraction (GIXRD) was performed on a Panalytical Empyrean diffractometer (GQ–CAC–CNEA), using a fixed incidence angle of 0.5°.

Transmission electronic microscopy (TEM) was performed using a Philips EM301 operating at 60 kV. Samples were scratched off from the substrate and deposited on carbon-coated copper grids (EMS).

Fourier-Transform Infrared Spectroscopy (FTIR) mesurements were performed using a JASCO FT-IR 4700, on samples deposited on fused silica and silicon substrates. The spectra were obtained using 512 individual scans for each measurement, and a resolution of 2 cm^{-1}.

NMR experiments were performed on a Bruker Biospin AVIII600 (600MHz) at IQUIMEFA (FFyB–UBA–CONICET). A 1.1 m $AlCl_3$ solution in water was used as an external reference for ^{27}Al experiments. Small amounts of perdeuterated acetone were added to the samples for signal lock.

Transmission UV-Vis-NIR spectrometry was measured on samples deposited on fused silica substrates, using a Hewlett Packard 8452 diode array spectrophotometer and 1 nm resolution.

3. Results & discussion

3.1. Mesoporous Films

The integration of porous aluminium oxide thin films into devices requires a precise determination and control of the properties of the material. The most important parameters

of design are the thickness and effective refractive index, which is modulated by the film porosity. Each of these items was studied in detail.

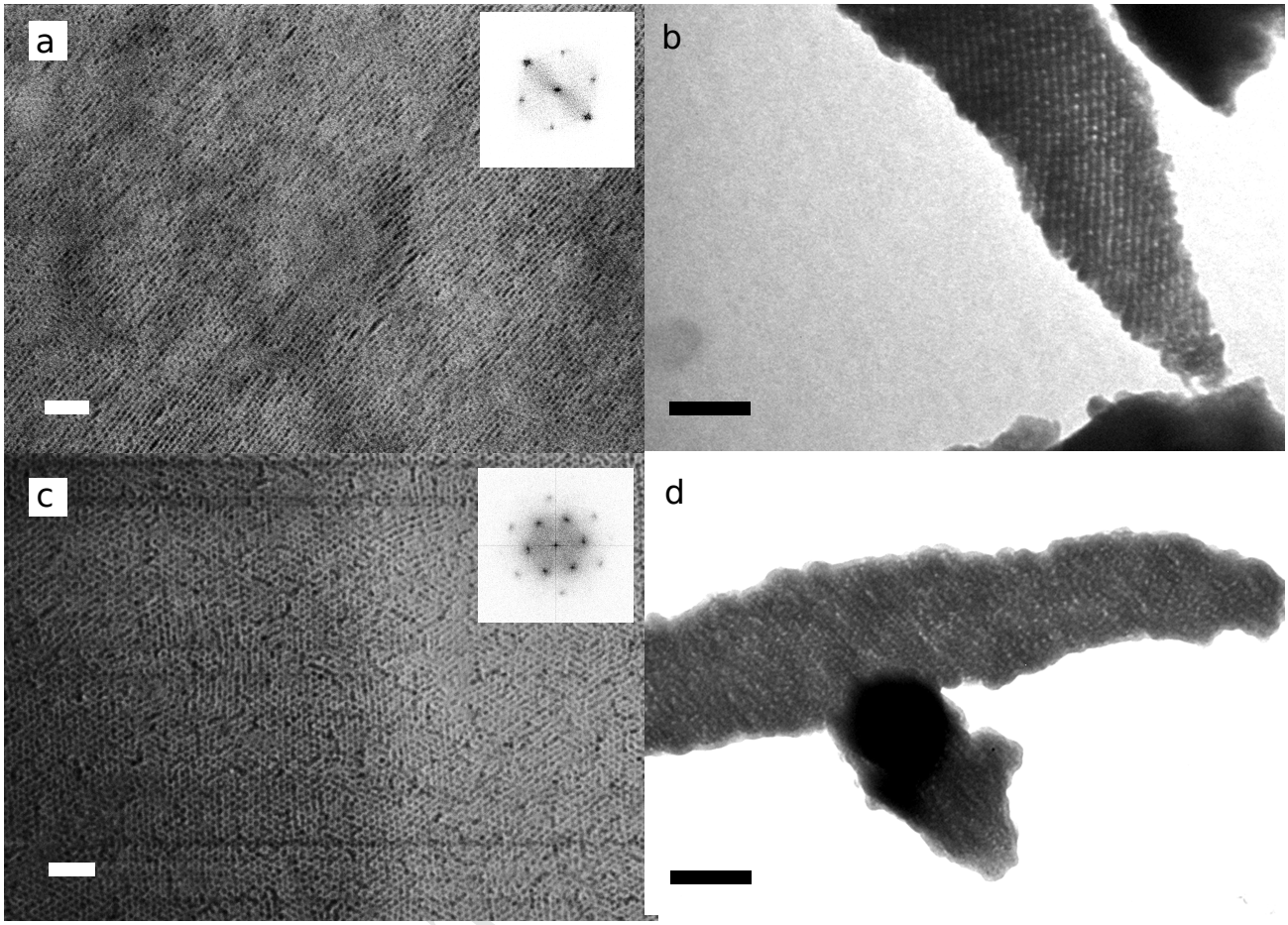

Figure 1: Typical FESEM (a,c) and TEM (b,d) images of films prepared using a,b) F127 and c,d) P123 as templates. The scale bars represent 100 nm. The insets show FT of the FESEM images.

3.1.1. Pore order.

The surface of films prepared using both templates show large domains of well-ordered pores. Figure 1 presents FESEM and TEM images of films prepared using F127 and P123 as templates. These images show the typical textures of $Im\bar{3}m$ and $Fm\bar{3}m$ mesopore arrangements for each of these templating agents, respectively. Although the uniaxial contraction distorts the cubic arrangements, we keep the nomenclature and indexing of the initial cubic order for simplicity. Films produced using F127 as template usually exhibit an $Im\bar{3}m$ pore arrangement, which usually lies with a direction of the [110] group perpendicular to the substrate. The pores in the exposed (110) plane exhibit two different characteristic distances, showing a "2+4" pseudo–hexagonal pattern[18] that is observed in the Fourier Transform (FT) of the image presented in the inset of Figure 1a. The stripes observed in the images

correspond to $\{\bar{1}10\}$ planes, and show a characteristic distance of 11.7 ± 0.8 nm. TEM images of these films (Figure 1b) show series of stripes with periodic thickness variation. This structure is typical of $Im\bar{3}m$ mesoporous materials observed through the $\langle 110 \rangle$ direction. Each clear stripe is formed by the superposition of pores of a plane of the $\{\bar{1}10\}$ family along different $\{110\}$ planes. The stripes show a characteristic distance of 12.0 ± 0.7 nm which is in agreement with that observed in FESEM.

When P123 is used as a template, usually an $Fm\bar{3}m$ pore arrangement is obtained. In this case it is normally a direction of the [111] group which lies perpendicular to the substrate, exposing one of the $\{111\}$ planes. The pores in these planes have hexagonal symmetry, as is observed on the Figure 1c. The long-range order and large size of pore domains produces up to fourth order peaks in the FT of the image (see inset). The interpore distance as measured in the image is of 15.5 ± 0.8 nm. Since the $\{111\}$ planes intersect the cubic cell through the diagonals, this interpore distance corresponds to a cell parameter of 21.9 ± 1.2 nm. The characteristic distance as recovered by the FT first order peak is 13.4 ± 0.5 nm, which corresponds to the $\{\bar{1}11\}$ planes. This yields a cell parameter of 21.9 ± 0.9 nm, which is consistent with the measured interpore distance. TEM images (Figure 1d) show a typical pattern of hexagonal symmetry, which correspond to the projection of pores of different planes of the 110 group through the $\langle 111 \rangle$ direction.

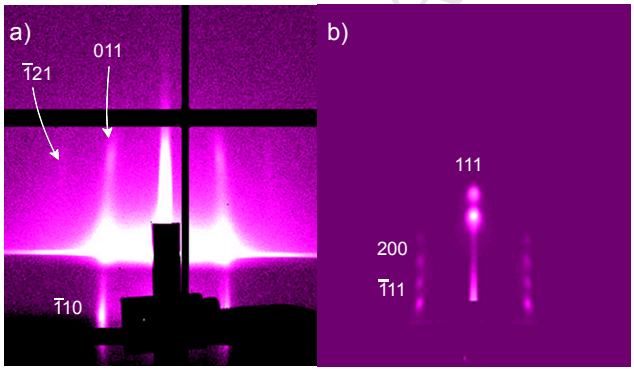

Figure 2: a) Combined transmission SAXS/GISAXS ($\alpha_i = 3°$) of a film prepared using F127 as templating agent and treated at 350 °C. The film was deposited on a thin substrate. b) GISAXS ($\alpha_i = 0.20°$) of a film prepared using P123 as templating agent and treated at 200 °C. The intensity scale is logarithmic in both images.

GISAXS and transmission SAXS experiments confirm the proposed pore arrangement for the films. The indexation and interpretation of the characteristic patterns generated by different pore arrangements has been already presented in the paper by Tate *et. al.*, in which our analysis is based. The high contraction after calcination at 350 °C makes observation of reflections with q_z component difficult. GISAXS of calcined samples performed on laboratory facilities show only lateral reflections for F127 templated films. Experiments performed in a synchrotron source (Figure 2a) show reflections corresponding to the $\{\bar{1}10\}$, $\{011\}$ and $\{\bar{1}21\}$ planes of a uniaxially oriented $Im\bar{3}m$ arrangement. The uniaxial contraction brings the (110) planes closer, while the $\{\bar{1}10\}$ planes distance is not affected since the film is

anchored to the substrate. This anisotropic contraction distorts the $Im\bar{3}m$ pattern making reflections with q_z component to appear at larger angles. The (110) reflection is not visible in this geometry since the intersection of the Ewald sphere with the reciprocal space points is minimal. The contraction of the film from the moment the $Im\bar{3}m$ arrangement forms up to the final dimensions can be measured through the differences in interplanar distances calculated from the GISAXS pattern. The $(\bar{1}10)$ plane shows a distance of 12.3 ± 0.3 nm, while the (011) plane shows a distance of 4.6 ± 0.5 nm. Based on these parameters, the (110) planes are expected to be at ≈ 2.3 nm, suggesting a contraction on the z plane of 80% from the initial cubic arrangement.

GISAXS of films prepared using P123 as template and calcined at 350 °C show very weak signals. In this case, no pure lateral ($q_z = 0$) reflection is expected. The high contraction degree expands the reciprocal lattice in the z direction, bringing the lattice points out of diffraction condition. In order to limit this effect, studies were performed on films heated only up to 200 °C (Figure 2b). In this case the pattern corresponds to a uniaxially oriented $Fm\bar{3}m$. Spot pairs coming from the (111), {200} and $\{\bar{1}11\}$ reflections are observed.[19] The retention of the periodic structure in the FESEM images of the films surfaces suggests that the order is maintained even after calcination at 350 °C.

It is important to note that no diffuse halo is observed in the GISAXS patterns for neither templating agent. That feature is commonly found in films where a mixture of a long-range ordered phase and an only first-neighbor ordered phase exist. The ordered phases usually are found next to the interfaces (air-film and film-substrate), while the disordered phase is found in the middle of the film. Although GISAXS does not homogeneously sample the whole thickness, partial order should show as a continuous halo in the pattern.

The pore arrays show large ordered domains in the xy plane. The borders between different domains are clearly visible on low magnification FESEM images. FT analysis of the pore order on each domain and the low roughness observed by XRR (*vide infra*) confirm that these features come indeed from the different pore orientations and are not due to thickness variations (see Figure S1).

3.1.2. Porosity.

The porous volume was measured by XRR and EEP. In both cases, the dielectric properties of the film are evaluated at different states of capillary water condensation. When X-rays are used as a probe, the amount of water condensed in the pores is related to changes in the average electronic density of the film, which has a direct correlation to the critical angle of total reflection. The critical angles were determined using a modified Bragg equation. Full details of XRR data analysis can be found in the overview by van der Lee.[20] Figure 3 shows extcolorredtypical reflectograms of F127 and P123 templated films at low (5–10%) and high (90–95%) RH values. The difference in the average electronic density between the film with pores empty and full of water produces a large shift in the critical angle, indicating that a high porous volume is accessible to water. This shift can be used to calculate the adsorbed water per unit volume, and thus the accessible porosity. Using this method, the accessible measured porosity lies between 40 and 60% for films prepared with either template.

The detection by XRR of the diffraction peak due to pore periodicity is hindered by the high contraction of the films. There are two reasons why this structural change makes it very difficult to see these peaks. Firstly, the decrease in the characteristic distance shifts the peak to larger angles, where specular reflectivity is very low and diffuse reflectivity dominates. Secondly, the contrast is strongly reduced by the contraction, leading to a very low modulation. An extreme example of this effect are the grid-like structures as reported by Sakatani *et al.*,[21] and also studied later by our group.[22] The fact that signals with nonzero q_z component are very weak in the GISAXS is consistent with the absence of the diffraction peaks.

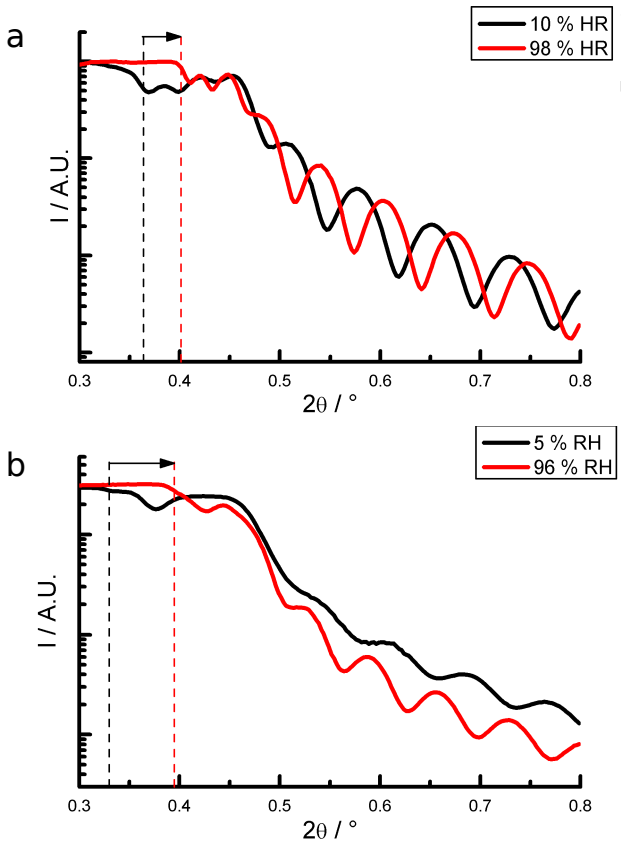

Figure 3: Typical XRR showing the critical angle shift of films measured under low and high humidity. a) F127 and b) P123 templated films of 100 nm and 101 nm respectively.The dotted lines show the position of the critical angles, and the arrows show their shifts.

Figure 4 shows the results for ellipsometric measurements on F127 templated films. The effective refractive index of the films at 630 nm varies from 1.30 for empty films up to 1.53 when the pores are filled with water. The adsorption isotherm shows a steep increase on the adsorbed volume both on the adsorption and desorption branches, showing H1 character. This kind of isotherm indicates that the pores are highly interconnected, with a slit-like shape. The large contraction on the z direction produces the partial coalescence of planes of

pores, showing an almost grid-like texture on the surface (Figure 1), resulting on thin slabs of material separated by slit-shaped pores. The characteristic pore radii derived from the isotherm, using a simple Kelvin model, are 4.1 ± 0.4 nm for adsorption and 2.3 ± 0.2 nm for desorption. The pore volume measured by this method is slightly less than 60%, confirming that the film pores are highly accessible. In the case of films prepared with P123 as a template, the presence of a large radius of curvature precludes the filling of the pores. In this case it was instrumentally not possible to measure a hysteresis loop event at RH larger then 90%.

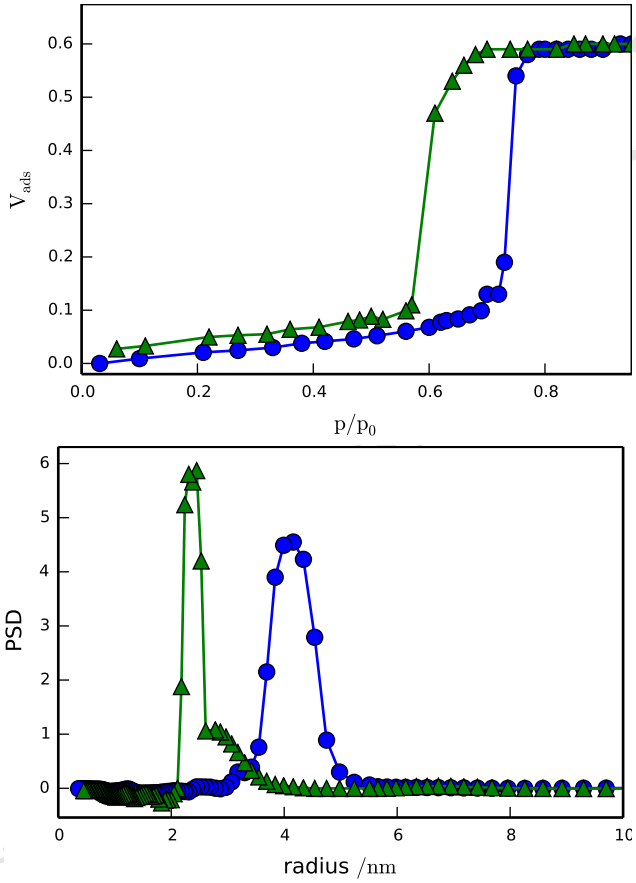

Figure 4: Adsorption isotherm and derived pore size distribution for a F127 templated film. Circles correspond to adsorption and triangles to desorption. The lines are just guides to the eye.

3.1.3. Thickness control.

Film thickness is controlled by varying both the deposition conditions (withdrawal or spin rates) and the total concentration of the sol (represented through the ethanol:Al ratio, see the experimental section). Figure 5 shows the measured thicknesses for dip-coated films prepared using three different concentrations and four different withdrawal rates, for each templating agent. When the ethanol:Al ratio is low, high withdrawal or low spin speeds produce thick films that do not withstand the internal stresses developed during

thermal treatment. In these cases cracking takes place, sometimes leading to optical quality degradation (see Figure S2). The highest acceptable withdrawal speed decreases when the ethanol:Al ratio decreases. For both surfactants employed, sols with ethanol:Al ratios of 40:1 casted at 2.5 $\mathrm{mm \cdot s^{-1}}$ and higher withdrawal speeds develop cracks, while for 100:1 ratios continuous and crack-free films can be casted at 4.0 $\mathrm{mm \cdot s^{-1}}$. The films have low surface roughness, as required for high optical quality films. The presence of fringes between the film and substrate critical angles on XRR measurements (see Figure 3) is characteristic of very uniform films. XRR fitting shows that roughness is less than 1.5 nm for all measured films.

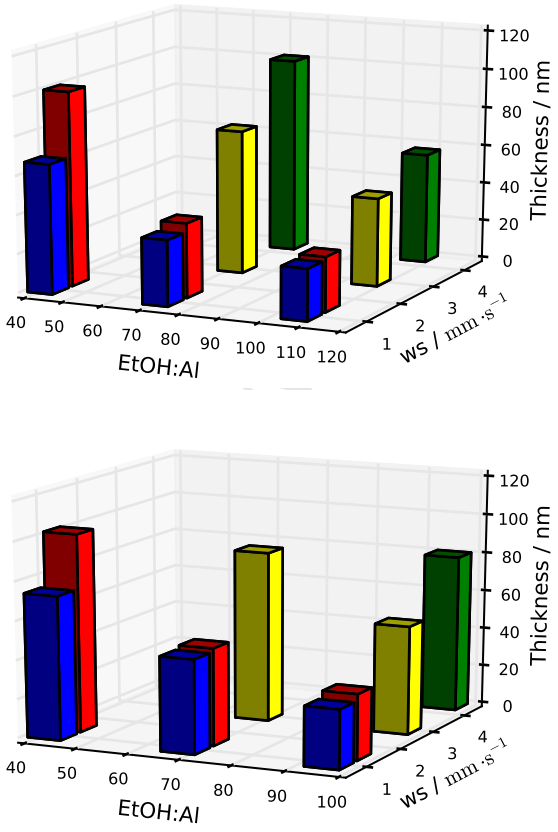

Figure 5: Thickness of films prepared using a) F127 and b) P123 as templates, using different EtOH:Al ratios. The withdrawal speeds (ws) are 0.5, 1.0, 2.5 and 4.0 $\mathrm{mm \cdot s^{-1}}$.

Varying the withdrawal speed from 0.5 $\mathrm{mm \cdot s^{-1}}$ to 4.0 $\mathrm{mm \cdot s^{-1}}$ and the total ethanol:Al ratio from 40:1 to 90:1, the thickness can be controlled from $\approx$ 30 nm up to $\approx$ 100 nm for films prepared using either templating agent. Further dilution of the sols could provide thinner films.

3.1.4. Optical properties.

In order to be useful for applications in optical devices, the films must show a good transparency over the widest possible wavelength range. The transparency is affected not only by optical adsorption but also by scattering. Cracks and thickness or refractive index inhomogeneities in the scale of the wavelength produce a strong light scattering, reducing transparency. In the UV range, these requirements impose strict conditions on the film properties. Our results show that the films are very homogeneous and of excellent optical quality. UV–Vis–NIR spectrum (Figure 6) show that the films are transparent right from 200 nm at least up to 1100 nm. As expected for a thin film of lower refractive index than the substrate, the transparency of the system is increased after coating. The optical parameters were measured using spectroscopic ellipsometry measurements in the range 300–960 nm. Due to the high porosity of the films, the refractive index is very low (1.297 at 630 nm for F127 and 1.161 for P123). The dispersion relation for F127 templated films can be modelled using a Cauchy relationship with parameters $A = 1.283$ and $B = 5.64 \times 10^{-3}\,\mu\text{m}^2$, while for P123 templated films the refractive index can be modelled using parameters $A = 1.160$ and $B = 5.51 \times 10^{-4}\,\mu\text{m}^2$.

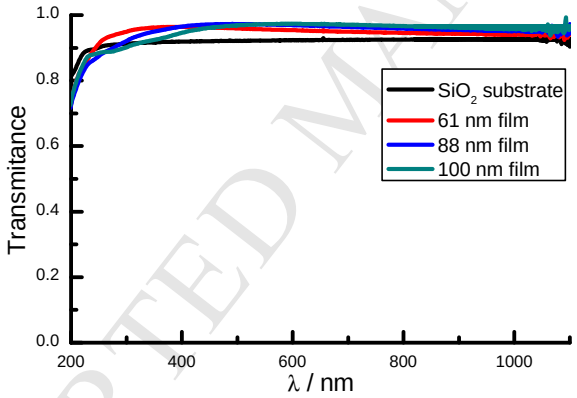

Figure 6: UV-Vis-NIR transmission spectra of F127 templated films of different thicknesses deposited on SiO_2 and of a bare SiO_2 substrate.

3.2. Evolution during the sol-gel process

The condensation chemistry of Al^{3+} requires controlled conditions in order to compatibilize its sol-gel transition kinetics and the coassembly with surfactant micelles. Different approaches have been employed to control the aluminium hydrolysis and condensation rates in EISA processes. They can be globally categorized in three strategies: a) complexation and acidification of alkoxides, b) basification of salts and c) precondensed nanobuildingblocks (NBBs).

As examples of the first strategy, De *et al.* adapted the synthetic conditions they used for xerogels[23, 24] to prepare mesoporous thin films.[25, 26] Triblock copolymers were used as structure directing agents, 2,3-pentenedione as a hydrolysis control agent and HNO_3 to

inhibit condensation. In this synthesis, an important aging effect is observed in the mesopore order.[26]

When using salts as precursors, the high acidity of the aluminium ion ($pK_a(Al^{3+}) \approx 5$)[27] greatly inhibits condensation and gelification. As a consequence, a base must be added to adjust the pH. Most works using salts as precursors employ NH_3 as a base, since it is readily eliminated during calcination. One of the first examples of this approach used Brij58 as a templating agent, $AlCl_3$ as the aluminium source and NH_3 to adjust the acidity.[28] They found that in absence of base the mesopore arrangement is unstable and is lost over time. Later, the same strategy was successfully applied to films templated using the KLE block copolymer.[29] More recently, a xerogel synthesis based on salts and organic acids as complexing agents[30] was employed for the preparation of mesoporous thin films.[31] Although the pores showed good ordering, X-Ray reflectivity experiments showed that the thickness is highly inhomogeneous (roughness ≈ 16 nm).

Other strategies involve the preparation of preformed crystalline nanoparticles as NBBs. Either by *in situ* water generation[32] or chloride scavenging.[33] For example, *tert*-butanol has been used as a scavenger in the preparation of a sols comprised of crystalline titania nanoparticles.[14] These pathways require a lengthy NBB preparation or a very precise timing between reagents mixing and film deposition.

In this work we use *tert*-butanol as a stable scavenger, convenient for laboratory scale thin film production. Under high acidity conditions, this tertiary alcohol is protonated and dehydrates. The resulting carbocation reacts with chloride, raising the pH. This reactant is stable under normal conditions, maintaining a low pH until the EISA process takes place. Moreover, compared to other reagents that act as bases, like ammonia or epoxides, it is much easier to handle, being less volatile, toxic and reactive. Under the proposed experimental conditions the amount of reacted alcohol remains low until solvent evaporation takes place during deposition. As acid concentration increases, the alcohol is converted to the more volatile chloride, lowering the acidity and promoting condensation.

The classical EISA process picture involves the assembly of sol-gel precursors around templating entities, like the surfactant micelles used in this work. Depending on the nature of the reagents and on hydrolysis and condensation rates, these precursors can be either polymeric species or NBBs. For example, polymeric species are typical when using silicon alkoxides or phenol–formaldehyde resins (usually called "resols") as precursors. Conversely, NBBs are usually involved on the sol–gel synthesis of most 3rd and 4th row transition metal oxides. In order to elucidate the chemical nature of the material during the whole sol-gel process, we analysed the sol and the deposited gel at various processing stages.

3.2.1. Chemical nature of the sol.

Several NMR experiments were pursued in order to evaluate the chemical evolution of the sol, in particular the nature of the precursor species formed in the different stages of sol preparation. We covered the whole procedure, from the dissolution of aluminium trichloride in water up to the point of having a sol ready for deposition. Many of the experiments were focused on ^{27}Al NMR. This nucleus is quadrupolar and usually exhibits broad signals. Nevertheless, some species in which the Al is in a highly symmetric environment show very

sharp peaks. The best documented case of such behaviour is the formation of a tridecamer at high dilution and hydrolysis ratios (water to metal ratios) higher than 2.4.[27]

The stages of sol preparation that were evaluated are: a) dissolution of aluminium trichloride in water, b) previous solution with added *t*-BuOH, c) previous solution warmed at 50 °C for 15 minutes and d) previous solution diluted 20 times with ethanol.

Our results (Figure S3) show that in the sol a very low degree of condensation has occurred, and thus most of the aluminium species are monomeric. Furthermore, only a small portion of *t*-BuOH has reacted forming *tert*-butyl chloride.

The ^{27}Al spectra are similar at all evaluated stages, consisting of a peak centered at 0 ppm with a very small shoulder downfield that is compatible with a low amount of oligomers. The most significant result of ^{27}Al NMR is the complete absence of the 62.5 ppm signal from the Al tridecamer, an indication that in spite of the high hydrolysis ratio (H_2O:Al $\approx 20:1$) the acidity remains high enough to prevent extensive condensation.

The ^{1}H spectrum of $AlCl_3$ in water shows two extremely broad signals centered at 8.5 ppm and 5.0 ppm. These signals correspond to Al-bound and free water respectively. The high concentration and fast proton exchange between free and Al-bound water produces broadening of both signals. After adding *t*-BuOH, a single signal at 1.05 ppm from the methyl groups appear in the spectra. ^{13}C NMR shows the presence of C in two different environments, namely the methyls at 30.5 ppm and the tertiary carbon at 69.7 ppm. After heating, only a small amount of *t*-BuOH is converted to the corresponding chloride, as evidenced by the appearance of a peak at 34.14 ppm in the ^{13}C spectrum and a peak at 1.47 ppm in the ^{1}H spectrum, both corresponding to the *t*-butyl chloride methyl groups . The peak in the ^{1}H spectrum is partially overlapped with the one arising from the *t*-BuOH methyl groups, ruling out a precise integration. Nevertheless, a rough estimation suggests that only 1 % of the alcohol has reacted to form the chloride. The small amount of the chloride and lower sensitivity of the tertiary carbon impedes the detection of the corresponding signal in the ^{13}C spectrum.

Diluting with ethanol produces dramatic changes in the H_2O resonances. Signals coming from both bound and unbound water sharpen, giving rise to a moderately sharp signal of free water at 5.09 ppm and a broad signal at 9.56 ppm from bound water. These changes indicate that the dynamics of both proton and water exchange are much slower in this environment.

We postulate that the majority of the reaction of *t*-BuOH with chloride is triggered by solvent evaporation during deposition. The loss of solvent increases the acidity and metal concentration, leading to the formation of *t*-butyl chloride, producing extended condensation only after the film has been casted and the self assembly of the micelles has occurred. This hypothesis is based on some experimental observations: if films are prepared without citric acid spherulitic crystallization, probably of a pseudobohemite phase, takes place immediately after the film dries. In contrast, films prepared without *t*-BuOH are very hygroscopic and do not dry at room temperature. Indeed IR analysis of the films after heating at 60 °C (Figure 7) showed a strong and well-defined peak at 3052 cm^{-1} on films prepared with *t*-BuOH, which seems to arise from −OH vibrations of a pseudobohemite phase. The spectra of films prepared without *t*-BuOH presented a much less defined −OH environment. With the incorporation of citric acid, the signal centered at 3050 cm^{-1} is replaced by a broad

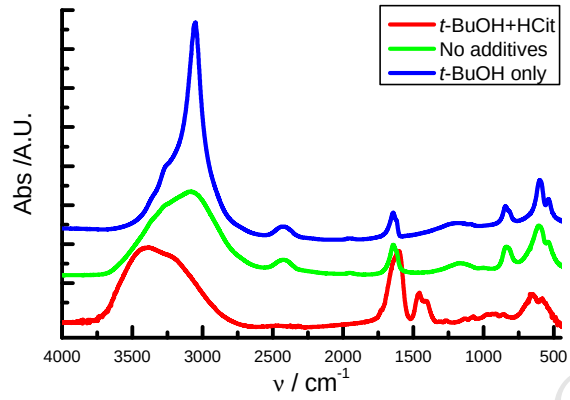

Figure 7: FTIR spectra of films deposited from sols without *t*-BuOH or citric acid, with *t*-BuOH only, and with both reactants. The films were treated 2 h at 60 °C before measurements. The spectra were shifted for clarity.

peak at 3400 cm^{-1}, that corresponds to bound water. Finally, experiments dissolving *t*-BuOH on HCl solutions (pH=1) showed that only minimal pH changes happen even after heating at 50 °C for 1 h. Thus, it is very likely that the reaction only proceeds to a small extent while the sol keeps its original composition, and only after much of the solvent has evaporated extensive chloride consumption takes place. This pathway is very different from that already developed for more acidic metal centers,[14] since in those cases the reaction takes place during sol preparation while in the present case most of the alcohol remains unreacted until deposition.

3.2.2. The as-prepared film is dynamic.

After the EISA process,[4, 5] a lightly condensed film is usually obtained. Depending on the nature of the metal center, and the amount of acids and complexing agent remaining, oxo and hydroxo bridges exist in the gelled material. Since the gel is not fully condensed, storing the as–deposited films at controlled humidity before calcination usually improves pore ordering by maintaining fluidity of the film at a mesoscopic scale. This treatment allows the surfactant molecules to diffuse, leading to better arrangement of the mesopores.[34] In the case of aluminium, as with other +3 metals, extensive olation is expected. Consequently, hydrated oxo-hydroxides form, that are prone to redissolution–reprecipitation.

Indeed, when we deposit films by dip-coating, large ordered domains are observed. The size of the domains is much larger in the case of films treated at 50 %RH than in films that were heated shortly after deposition. The domain size is also larger for films deposited at lower withdrawal speeds. As an example, in F127 templated films deposited at $1mm \cdot s^{-1}$ the domain area is between 15 to 20 μm^2 for films treated at controlled RH while it is only around 2 μm^2 for as-deposited films.

As is shown in Figure 8, the effect of the controlled humidity treatment on spin-coated samples is much more drastic: since the humidity in the spin-coater is very low (see experimental) the solvent is evaporated before the surfactant has assembled, so the EISA process

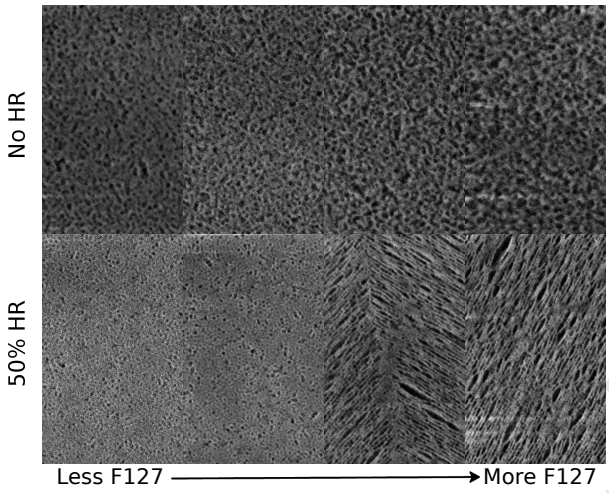

Figure 8: FESEM images of films prepared by spin coating with and without 50 %RH treatment. The F127:Al ratio vas varied from 2×10^{-3} to 6×10^{-3}.

does not take place. Samples prepared with F127 to Al ratios ranging from 2×10^{-3} up to 6×10^{-3} show similar textures if the RH treatment is omitted (upper part of Figure 8). The films are composed of aggregated particles separated by irregular pores of non-uniform size distribution. If the samples are exposed to 50 %RH before the thermal treatment, the fluidity of the film allows an extensive reorganization to take place, leading to shaping and ordering of the pores, finally rendering well-ordered films if the surfactant to metal ratio is adequate. During dip-coating the environmental humidity can be controlled, leading to a wider range of accessible deposition conditions. Moreover, the continuous draining of the sol leads to a steady-state system in which evaporation is much closer to equilibrium than during spin–coating. Using dip–coating and RH between 40 and 50% well-ordered films are obtained even subjecting the samples to thermal treatment, skipping the controlled RH step. The low humidity on the spin-coater leads to an initially more condensed oxide, and thus less dynamic and prone to reorganize mesophases than those obtained by dip–coating. Indeed, the mesopore arrangement domain sizes of spin-coated films is much smaller than those of films deposited by dip-coating, showing that although the film keeps its fluidity the structural rearrangement is limited. Raising the sol H_2O:Al ratio to 50, films with well ordered pores can be deposited by spin coating even without posterior RH treatment. Nevertheless, we have observed that with ratios over 100, a mixture of mesopore arrangements is obtained. The sol composition should thus be adjusted to match a particular deposition system.

3.2.3. Temperature evolution.

The as–deposited films are hybrid materials comprised of an inorganic phase including the organic surfactant micelles as templates. It is very likely that right after casting, the composition of the inorganic phase is a mixture of hydrated aluminium oxide hydroxide and citrate. This phase dehydrates and condenses, going from hydroxide to oxide phases, losing

the citrate at high temperatures. The gradual thermal treatment is required in order to provide mechanical strength through condensation and thus preserve the pore ordering: if the films are treated directly at 200 °C after deposition, a disordered structure of ill-defined pores is obtained. We studied the evolution of the thickness and nature of the films at different stages of the thermal treatment.

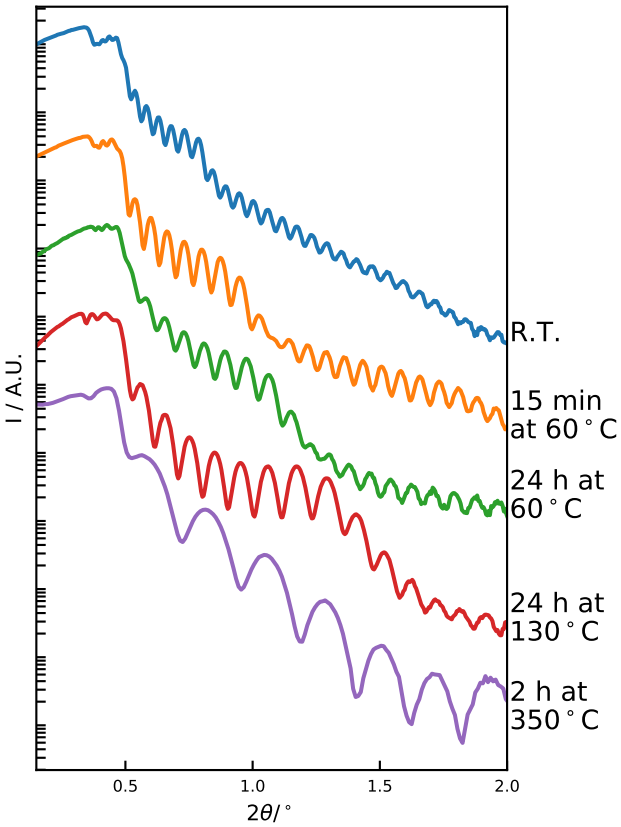

Figure 9: XRR patterns of films during various stages of thermal treatment. From top to bottom: as prepared, after 15 min at 60 °C, after 24 h at 60 °C, after 24 h at 130 °C, after calcination at 350 °C. The final thickness of the film is 38 nm. The reflectograms were shifted for clarity.

Thickness evolution. The thickness of a film was monitored by XRR at different steps of the thermal treatment: a) just after deposition, b) after 24 h at 60 °C, c) after 24 h at 130 °C and finally d) after 2 h at 350 °C. As shown in Figure 9, the thickness monotonically decreases as the temperature of thermal treatment increases. Simultaneously, the Bragg peak produced by the periodic order of the mesopores shifts from low to high-angles as the pore planes come closer.

After deposition and drying in the dip–coater, before any thermal treatment, the film is 144nm thick. The reflectograms show two critical angles. The one at lower angles correspond to the interface between air and the film. The higher critical angle is due to the film-substrate

interface. Between both critical angles, fringes are observed due to waveguiding inside the film. The presence of this resonance effect between both critical angles is a signature of films with very low roughness. Upon heating at 60 °C the thickness decreases with time, going from a 79 % of the initial thickness after 15 min to 72 % after 24 h. The film further contracts to 58 % after treatment at 130 °C for 2 h. At this temperature the critical angle decreases a little, possibly because of the loss of water that creates microporosity in the film. After calcination at 350 °C, an abrupt contraction takes place, resulting in a 38 nm thick mesoporous film, only a 26 % of the initial thickness. This contraction occurs with loss of surfactant and water, both occluded and due to formation of oxo-bridges instead of hydroxy bridges. Although the electronic density of the mesoporous walls increases due to densification, the loss of organic matter leaves empty mesopores, resulting in an electronic density similar to the one observed before calcination. The contraction of 74 % after the whole thermal treatment is consistent with the one estimated from GISAXS (80%). The small difference is very likely due to the fact that the porous arrangement has already been distorted by contraction when the XRR measurement of the as-prepared sample is performed.

Microstructure evolution. The microstructure was monitored by IR on samples deposited on fused silica and silicon substrates. Both samples with and without templating agents were studied, showing similar results.

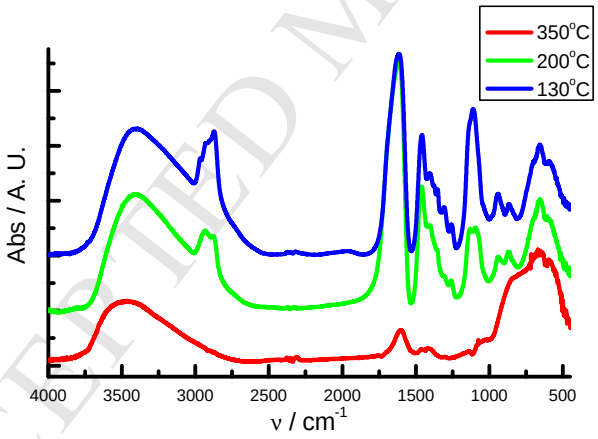

Figure 10: FTIR of films prepared using HCit, after being treated at (from top to bottom): 130 °C, 200 °C and 350 °C. The spectra were shifted for clarity.

Figure 10 shows the FT-IR spectra of templated films after treatment at 130, 200 and 350 °C for 2 h. At 130 °C, the signals from adsorbed water (3200-3400 cm^{-1}, 1600 cm^{-1}), surfactant (2870-2970 cm^{-1}, 1460-1250 cm^{-1}, 1100 cm^{-1}), citrate (1600 cm^{-1}, 1458 cm^{-1}, 1412 cm^{-1}) and Al−O (656–575 cm^{-1}) are present. This last broad signal suggests that at least some condensation of the oxide network has already occurred at this temperature. Between 800 and 1100 cm^{-1}, a complex set of peaks coming from citrate fingerprint is also visible in films prepared without surfactant. These signals are completely obscured in mesostructured films by those of the templating agent.

Upon heating at 200 °C, only small changes in the surfactant signals are observed. These changes are probably due to partial dehydration of the sample. Since the PEO-PPO-PEO copolymers used as templates are good acceptors for hydrogen bonding, the changes in the environment inside the mesostructured film produces small shifts in the position and intensity of the peaks. After calcination at 350 °C, the template is largely eliminated, as evidenced by the dissapearance of the C−O and CH_2 signals around 1100 and 2900cm^{-1}. The fingerprint of the Al−O−Al network widens from 656–575 cm^{-1} to 870–550 cm^{-1}, showing that further condensation takes place, and that an increase in the number of tetrahedral coordination sites happens at this temperature.[35] Due to the high surface area, signals of strongly adsorbed water remain at 1600 and 3500 cm^{-1}.

It is interesting to note that our analysis is different to the one performed on related systems by Eckhardt *et. al.*[36] This group prepared sols with a much higher citric acid to aluminium ratio (eight times the one used on this work), and without a proton scavenger. In that work signals observed at 1608 and 1469cm^{-1} were assigned to aluminium carbonate produced after citrate decomposition. We assign the signals at 1614 and 1456 cm^{-1} to Al-bound citrate. IR spectra of non-templated samples show no evidence of citrate decomposition up to at least 200 °C (see Figure S4). Indeed, these signals are present at similar positions even on samples that have not been heated. Although there is a possibility that citrate and carbonate IR signals coincide, further experiments should be performed to confirm this hypothesis.

The low sample mass and the low reflecting power of aluminium oxides makes it difficult to determine the crystalline phase of these films using XRD. GIXRD shows diffuse dispersion for samples treated at 350°C. When the samples were heated to 1000°C, very weak reflections that can be assigned to a γ phase were observed (See Figure S5).

4. Conclusions

A robust method for the synthesis of mesoporous aluminium oxide thin films has been presented. The method relies on a simple and innovative process for controlling the acidity during casting, using *t*-BuOH as a chloride scavenger. The procedure avoids the use of alkoxides, and toxic or difficult to handle reagents, resulting in an economical, safer and more robust method than previous alternatives.

Using the optimal surfactant to metal proportion, the films show large domains of ordered pores. The accessible volume is between 40% and 60%, leading to low refractive index films amenable to be used in antireflective coatings and devices requiring low-κ thin films.

Due to their very low roughness, the films show excellent optical quality, being transparent over a wide wavelength range going from UV to the NIR. The thickness can be controlled between tens of nanometers up to around 100 nm. This range is suitable for building optical devices based on mesoporous metal oxide thin films.

5. Acknowledgments

We would like to thank IQUIMEFA–FFyB for providing access to the NMR equipment, and Dr L. Fabian for kindly performing the experiments. M. Ceolin (INIFTA) is acknowl-

edged for kindly performing preliminar GISAXS experiments, and J. Morrone for kindly performing EEP measurements. Funding was provided by ANPCyT PICT 2015-3853. L.M.S.M acknowledges a CONICET Postdoctoral scholarship. A.Z., M.C.F. and P.A.H. are members of CONICET scientific staff. P. C. Angelomé is acknowledged for fruitful discussions and help with sample preparation and characterization and M. B de Alvarez for critical reading of the manuscript.

[1] J. Y. Ying, C. P. Mehnert, M. S. Wong, Synthesis and Applications of Supramolecular-Templated Mesoporous Materials, Angewandte Chemical International Edition 38 (1-2) (1999) 56–77.

[2] P. Innocenzi, L. Malfatti, Mesoporous thin films: properties and applications, Chemical Society Reviews 42 (9) (2013) 4198–4216. doi:10.1039/c3cs35377j.
URL http://xlink.rsc.org/?DOI=c3cs35377j

[3] Y. Ren, Z. Ma, P. G. Bruce, Ordered mesoporous metal oxides: synthesis and applications., Chemical Society reviews 41 (14) (2012) 4909–4927. doi:10.1039/c2cs35086f.
URL http://www.ncbi.nlm.nih.gov/pubmed/22653082

[4] C. J. Brinker, Y. Lu, A. Sellinger, H. Fan, Evaporation-Induced Self-Assembly: Nanostructures Made Easy, Advanced Materials 11 (7) (1999) 579–585. doi:10.1002/(SICI)1521-4095(199905)11:7¡579::AID-ADMA579¿3.0.CO;2-R.
URL http://doi.wiley.com/10.1002/(SICI)1521-4095(199905)11:7%3C579::AID-ADMA579%3E3.0.CO;2-R

[5] D. Grosso, F. Cagnol, G. J. A. A. Soler-Illia, E. L. Crepaldi, H. Amenitsch, A. Brunet-Bruneau, A. Bourgeois, C. Sanchez, Fundamentals of Mesostructuring Through Evaporation-Induced Self-Assembly, Advanced Functional Materials 14 (4) (2004) 309–322. doi:10.1002/adfm.200305036.
URL http://doi.wiley.com/10.1002/adfm.200305036

[6] D. Gu, F. Schüth, Synthesis of non-siliceous mesoporous oxides, Chem. Soc. Rev. 43 (1) (2014) 313–344. doi:10.1039/C3CS60155B.
URL http://xlink.rsc.org/?DOI=C3CS60155B

[7] F. Schüth, Non-siliceous Mesostructured and Mesoporous Materials, Chemistry of Materials 13 (10) (2001) 3184–3195. doi:10.1021/cm011030j.
URL http://pubs.acs.org/doi/abs/10.1021/cm011030j

[8] M. G. Kanatzidis, Beyond Silica: Nonoxidic Mesostructured Materials, Advanced Materials 19 (9) (2007) 1165–1181. doi:10.1002/adma.200601763.
URL http://doi.wiley.com/10.1002/adma.200601763

[9] H. Knözinger, P. Ratnasamy, Catalytic Aluminas: Surface Models and Characterization of Surface Sites, Catalysis Reviews 17 (1) (1978) 31–70. doi:10.1080/03602457808080878.
URL http://www.tandfonline.com/doi/abs/10.1080/03602457808080878

[10] F. Shan, A. Liu, H. Zhu, W. Kong, J. Liu, B. Shin, E. Fortunato, R. Martins, G. Liu, High-mobility p-type NiO_x thin-film transistors processed at low temperatures with Al_2O_3 high-k dielectric, J. Mater. Chem. C 4 (40) (2016) 9438–9444. doi:10.1039/C6TC02137A.
URL http://xlink.rsc.org/?DOI=C6TC02137A

[11] M. Nofz, Alumina Thin Films, in: Handbook of Sol-Gel Science and Technology, Springer International Publishing, Cham, 2016, pp. 1–44. doi:10.1007/978-3-319-19454-7_133-1.
URL http://link.springer.com/10.1007/978-3-319-19454-7_133-1

[12] M. E. Calvo, S. Colodrero, N. Hidalgo, G. Lozano, C. López-López, O. Sánchez-Sobrado, H. Míguez, Porous one dimensional photonic crystals: novel multifunctional materials for environmental and energy applications, Energy & Environmental Science 4 (12) (2011) 4800. doi:10.1039/c1ee02081a.
URL http://xlink.rsc.org/?DOI=c1ee02081a

[13] J. Y. Y. Loh, D. P. Puzzo, P. G. O'Brien, G. A. Ozin, N. P. Kherani, Enhancing photovoltaics with broadband high-transparency glass using porosity-tuned multilayer silica nanoparticle anti-reflective coatings, RSC Adv. 4 (59) (2014) 31188–31195. doi:10.1039/C4RA03465A.
URL http://xlink.rsc.org/?DOI=C4RA03465A

[14] J. M. Szeifert, J. M. Feckl, D. Fattakhova-Rohlfing, Y. Liu, V. Kalousek, J. Rathousky, T. Bein,

Ultrasmall Titania Nanocrystals and Their Direct Assembly into Mesoporous Structures Showing Fast Lithium Insertion, Journal of the American Chemical Society 132 (36) (2010) 12605–12611. doi:10.1021/ja101810e.
URL https://pubs.acs.org/doi/10.1021/ja101810e

[15] J. Daillant, A. Gibaud (Eds.), X-ray and Neutron Reflectivity, Vol. 770 of Lecture Notes in Physics, Springer Berlin Heidelberg, Berlin, Heidelberg, 2009. doi:10.1007/978-3-540-88588-7.
URL http://link.springer.com/10.1007/978-3-540-88588-7

[16] M. Klotz, V. Rouessac, D. Rébiscoul, A. Ayral, A. van der Lee, Adsorptiondesorption isotherms of nanoporous thin films measured by X-ray reflectometry, Thin Solid Films 495 (1-2) (2006) 214–218. doi:10.1016/j.tsf.2005.08.168.
URL http://linkinghub.elsevier.com/retrieve/pii/S0040609005013945

[17] M. R. Baklanov, K. P. Mogilnikov, V. G. Polovinkin, F. N. Dultsev, Determination of pore size distribution in thin films by ellipsometric porosimetry, Journal of Vacuum Science & Technology B: Microelectronics and Nanometer Structures Processing, Measurement, and Phenomena 18 (3) (2000) 1385–1391. doi:10.1116/1.591390.
URL https://avs.scitation.org/doi/abs/10.1116/1.591390

[18] G. J. A. A. Soler-Illia, P. C. Angelomé, M. C. Fuertes, D. Grosso, C. Boissiere, Critical aspects in the production of periodically ordered mesoporous titania thin films., Nanoscale 4 (8) (2012) 2549–2566. doi:10.1039/c2nr11817c.
URL http://www.ncbi.nlm.nih.gov/pubmed/22419250

[19] M. P. Tate, V. N. Urade, J. D. Kowalski, T.-c. Wei, B. D. Hamilton, B. W. Eggiman, H. W. Hillhouse, Simulation and Interpretation of 2D Diffraction Patterns from Self-Assembled Nanostructured Films at Arbitrary Angles of Incidence: From Grazing Incidence (Above the Critical Angle) to Transmission Perpendicular to the Substrate, The Journal of Physical Chemistry B 110 (20) (2006) 9882–9892. doi:10.1021/jp0566008.
URL http://pubs.acs.org/doi/abs/10.1021/jp0566008

[20] A. van der Lee, Grazing incidence specular reflectivity: theory, experiment, and applications, Solid State Sciences 2 (2) (2000) 257–278. doi:10.1016/S1293-2558(00)00119-9.
URL http://linkinghub.elsevier.com/retrieve/pii/S1293255800001199

[21] Y. Sakatani, D. Grosso, L. Nicole, C. Boissière, G. J. A. A. Soler-Illia, C. Sanchez, Optimised photocatalytic activity of grid-like mesoporous TiO2 films: effect of crystallinity, pore size distribution, and pore accessibility, Journal of Materials Chemistry 16 (1) (2006) 77–82. doi:10.1039/b512824m.
URL http://xlink.rsc.org/?DOI=b512824m

[22] I. L. Violi, M. D. Perez, M. C. Fuertes, G. J. A. A. Soler-Illia, Highly Ordered, Accessible and Nanocrystalline Mesoporous TiO 2 Thin Films on Transparent Conductive Substrates, ACS Applied Materials & Interfaces 4 (8) (2012) 4320–4330. doi:10.1021/am300990p.
URL http://pubs.acs.org/doi/abs/10.1021/am300990p

[23] D. Jana, G. De, Spontaneous generation and shape conversion of silver nanoparticles in alumina sol, and shaped silver nanoparticle incorporated alumina films, Journal of Materials Chemistry 21 (16) (2011) 6072–6078. doi:10.1039/c0jm03743e.
URL http://xlink.rsc.org/?DOI=c0jm03743e

[24] G. De, S. Bhattacharyya, Au nanoparticles in alumina sols and coatings, Journal of Materials Chemistry 18 (24) (2008) 2816–2824. doi:10.1039/b802156b.
URL http://xlink.rsc.org/?DOI=b802156b

[25] A. Mitra, D. Jana, G. De, A facile synthesis of cubic (Im3m) alumina films on glass with potential catalytic activity., Chemical communications (Cambridge, England) 48 (27) (2012) 3333–3335. doi:10.1039/c2cc18053g.
URL http://www.ncbi.nlm.nih.gov/pubmed/22362169

[26] A. Mitra, D. Jana, G. De, Facile synthesis of hexagonally ordered mesoporous aluminum oxide thin films with high catalytic activity, Microporous and Mesoporous Materials 158 (2012) 187–194. doi:10.1016/j.micromeso.2012.03.024.

URL http://linkinghub.elsevier.com/retrieve/pii/S1387181112001734

[27] C. F. Baes, R. E. Mesmer, The hydrolysis of cations, Wiley Interscience, 1976.

[28] L. Pidol, D. Grosso, G. J. A. A. Soler-Illia, E. L. Crepaldi, C. Sanchez, P. A. Albouy, H. Amenitsch, P. Euzen, Hexagonally organised mesoporous aluminiumoxohydroxide thin films prepared by the template approach. In situ study of the structural formation, Journal of Materials Chemistry 12 (3) (2002) 557–564. doi:10.1039/b109192c.
URL http://xlink.rsc.org/?DOI=b109192c

[29] M. Kuemmel, D. Grosso, C. Boissière, B. Smarsly, T. Brezesinski, P. A. Albouy, H. Amenitsch, C. Sanchez, Thermally Stable Nanocrystalline γ-Alumina Layers with Highly Ordered 3D Mesoporosity, Angewandte Chemie International Edition 44 (29) (2005) 4589–4592. doi:10.1002/anie.200500037.
URL http://doi.wiley.com/10.1002/anie.200500037

[30] Q. Yuan, A.-X. Yin, C. Luo, L.-D. Sun, Y.-W. Zhang, W.-T. Duan, H.-C. Liu, C.-H. Yan, Facile Synthesis for Ordered Mesoporous γ-Aluminas with High Thermal Stability, Journal of the American Chemical Society 130 (11) (2008) 3465–3472. doi:10.1021/ja0764308.
URL http://pubs.acs.org/doi/abs/10.1021/ja0764308

[31] G. J. B. Voss, E. A. Chavez Panduro, A. Midttveit, J. B. Fløystad, K. Høydalsvik, A. Gibaud, D. W. Breiby, M. Rønning, Mesostructured alumina as powders and thin films, Journal of Materials Chemistry A 2 (25) (2014) 9727–9735. doi:10.1039/c4ta00604f.
URL http://xlink.rsc.org/?DOI=c4ta00604f

[32] C. Weidmann, K. Brezesinski, C. Suchomski, K. Tropp, N. Grosser, J. Haetge, B. M. Smarsly, T. Brezesinski, Morphology-Controlled Synthesis of Nanocrystalline η-Al2O3 Thin Films, Powders, Microbeads, and Nanofibers with Tunable Pore Sizes from Preformed Oligomeric Oxo-Hydroxo Building Blocks, Chemistry of Materials 24 (3) (2012) 486–494. doi:10.1021/cm202692q.
URL http://pubs.acs.org/doi/abs/10.1021/cm202692q

[33] N. Tarutani, Y. Tokudome, M. Jobbágy, F. A. Viva, G. J. A. A. Soler-Illia, M. Takahashi, Single-Nanometer-Sized Low-Valence Metal Hydroxide Crystals: Synthesis via Epoxide-Mediated Alkalinization and Assembly toward Functional Mesoporous Materials, Chemistry of Materials 28 (16) (2016) 5606–5610. doi:10.1021/acs.chemmater.6b02510.
URL http://pubs.acs.org/doi/abs/10.1021/acs.chemmater.6b02510

[34] E. L. Crepaldi, G. J. d. A. A. Soler-Illia, D. Grosso, F. Cagnol, F. Ribot, C. Sanchez, Controlled Formation of Highly Organized Mesoporous Titania Thin Films: From Mesostructured Hybrids to Mesoporous Nanoanatase TiO 2, Journal of the American Chemical Society 125 (32) (2003) 9770–9786. doi:10.1021/ja030070g.
URL http://pubs.acs.org/doi/abs/10.1021/ja030070g

[35] G. Krishna Priya, P. Padmaja, K. G. K. Warrier, A. D. Damodaran, G. Aruldhas, Dehydroxylation and high temperature phase formation in sol-gel boehmite characterized by Fourier transform infrared spectroscopy, Journal of Materials Science Letters 16 (19) (1997) 1584–1587. doi:10.1023/A:1018568418302.
URL http://link.springer.com/10.1023/A:1018568418302

[36] B. Eckhardt, E. Ortel, D. Bernsmeier, J. Polte, P. Strasser, U. Vainio, F. Emmerling, R. Kraehnert, Micelle-Templated Oxides and Carbonates of Zinc, Cobalt, and Aluminum and a Generalized Strategy for Their Synthesis, Chemistry of Materials 25 (14) (2013) 2749–2758. doi:10.1021/cm400535d.
URL http://pubs.acs.org/doi/10.1021/cm400535d

ACCEPTED MANUSCRIPT

ACCEPTED MANUSCRIPT

- UV-Vis-NIR transparent mesoporous alumina thin films are easily prepared
- The thickness can be controlled between 30 and 100 nm
- The highly ordered porosity leads to very low refractive index films.
- A tertiary alcohol works as a chloride scavenger
- Condensation in inhibited until final stages of deposition

ACCEPTED MANUSCRIPT